

Banner appropriate to article type will appear here in typeset article

A hyperelastic oscillatory Couette system

Tejaswin Parthasarathy¹, Yashraj Bhosale¹, and Mattia Gazzola¹†

¹Mechanical Sciences and Engineering, University of Illinois at Urbana-Champaign, Urbana, IL 61801, USA

(Received xx; revised xx; accepted xx)

We report (semi-)analytical solutions of a problem involving a visco-hyperelastic solid material layer sandwiched between two fluid layers, in turn confined by two long planar walls that undergo oscillatory motion. The resulting system dynamics are rationalized, based on fluid viscosity and solid elasticity, via wave and boundary-layer theory. This allows for physical interpretation of elasto-hydrodynamic coupling, potentially connecting to a broad set of biophysical phenomena and applications, from synovial joint mechanics to elastometry. Further, obtained solutions are demonstrated to be rigorous benchmarks for testing coupled incompressible fluid–hyperelastic solid and multiphase numerical solvers, towards which we highlight challenging parameter sets. Finally, we provide an interactive, online sandbox to build physical intuition, and open-source our code-base.

Key words: flow–structure interaction, elastohydrodynamics, oscillatory flows, Couette flows, elastic waves

1. Introduction

We report (semi-)analytical solutions of a minimal, yet representative problem involving a visco-hyperelastic solid material layer sandwiched between two fluid layers, in turn confined by two long planar walls that undergo oscillatory motion (Fig. 1). We are motivated by the ubiquity and relevance of coupled interactions between viscous fluid and visco-hyperelastic solids in engineering and biology (Dowell & Hall 2001; Grotberg & Jensen 2004; Zhu & Jane Wang 2011; Heil & Hazel 2011; Barthes-Biesel 2016). Despite the numerous efforts to investigate this class of systems across modalities (theory, simulations, experiments) and applications, from vesicle transport (Pozrikidis 2003; Vlahovska & Gracia 2007), pulmonary (Grotberg & Jensen 2004; Heil *et al.* 2008), esophageal (Kou *et al.* 2017) or cardio-vascular systems (Li *et al.* 2013; Bodnár *et al.* 2014), biolocomotion (Argentina *et al.* 2007; Gazzola *et al.* 2015; Tytell *et al.* 2016), microfluidics (Wang & Christov 2019; Christov 2021), drag reduction or energy harvesting (Alben *et al.* 2002, 2004; Argentina & Mahadevan 2005; Bhosale *et al.* 2020), there is a perhaps surprising paucity of rigorous, analytical benchmarks that capture, in a minimal setting, tightly coupled, interfacially-driven dynamics between hyperelastic solids

† Email address for correspondence: mgazzola@illinois.edu

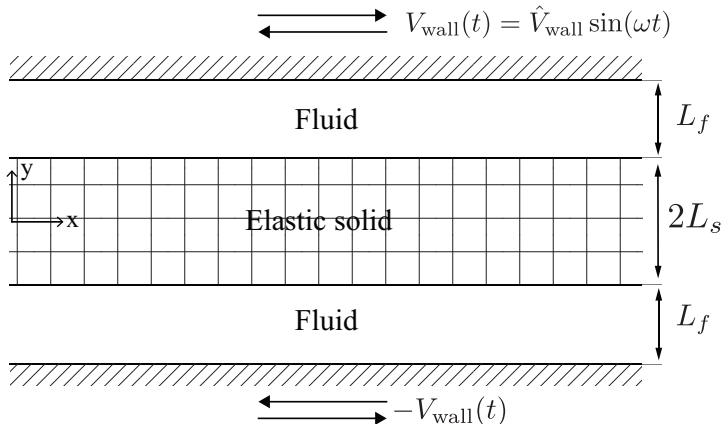


Figure 1: Schematic of the problem setup.

and shearing fluids. Such solutions are important to characterize relevant spatio-temporal scales, non-dimensional parameters and solution sensitivity, which are necessary for building intuition into practical flow–structure interaction problems.

Our setup, inspired by Sugiyama *et al.* (2011), caters to these requirements by coupling an incompressible Newtonian fluid to an incompressible density-mismatched visco-hyperelastic solid made of neo-Hookean and generalized Mooney–Rivlin materials, using a single, well-defined interface. By analyzing the flow field at this interface, we can understand the degree of dynamic coupling and mechanisms at play. This analysis is possible because in our setup the governing equations reduce to the simplest possible case of single dimension, while identically satisfying constraints of incompressibility. This results in decoupled algebraic equations which we solve to derive rigorous, analytical solutions. These solutions help isolate the spatio-temporal scales at play, and study parametric effects.

We begin by providing a detailed derivation of the flow solution, first in the case of a neo-Hookean solid, which in the limit of zero solid elasticity is shown to be consistent with classical multiphase Stokes–Couette flow solutions (Landau & Lifshitz 1987; Sim 2006; Leclaire *et al.* 2014). We then investigate the parametric impact of solid elasticity and fluid viscosity, and provide intuition for the observed results, using wave and boundary layer theory. These results are contextualized using applications in bio-engineering, from synovial joint mechanics to elastometry. During these parametric variations, we discover regimes marked by unusually high solid displacements, which we attribute to elastic, standing wave harmonics. We then carry forth our analysis from neo-Hookean solids to generalized Mooney–Rivlin solids, where closed-form solutions are no longer available. Here, to gain intuition into non-linear effects, we derive and analyze a semi-analytical solution.

Our setup also serves as a useful benchmark for validating fluid–elastic structure interaction and multiphase simulation codes, towards which we highlight challenging parameter sets, and comparisons with direct numerical simulations (Bhosale *et al.* 2021). Finally, to further build intuition, we provide an interactive, online sandbox and open-source our code.

The work is organized as follows: the problem setup and governing equations are introduced in Section 2; simplifications and analytical solutions for neo-Hookean solids are discussed in Section 3 with the corresponding system behavior presented in Section 4; (semi-)analytical solutions for Mooney–Rivlin materials and their interpretation are presented in Section 5; concluding remarks are provided in Section 6.

2. Problem setup and governing equations

A schematic of the setup is shown in Fig. 1, where we have a two-dimensional visco-hyperelastic solid sandwiched between two layers of fluid, such that the system is top-down symmetric. The thickness of the solid and each fluid layer is $2L_s$ and L_f , respectively. The setup is infinitely long and hence homogeneous in the x direction. The fluid is bounded by two planar walls which present a prescribed sinusoidal oscillatory motion $V_{\text{wall}}(t) := \hat{V}_{\text{wall}} \sin(\omega t) = \text{Im} [\hat{V}_{\text{wall}} \exp(i\omega t)]$, where hatted quantities denote the Fourier coefficients obtained upon a temporal Fourier transform, ω is the angular frequency of oscillations, and $T = 2\pi/\omega$ is the time period of oscillation. The bottom wall oscillates out of phase with the top wall, with phase shift π .

2.1. Governing equations

We consider a two-dimensional domain Σ physically occupied by elastic solid and a viscous fluid, with Ω_e & $\partial\Omega_e$ representing the support and boundaries of the elastic solid, respectively. The fluid region is represented by $\Sigma - \overline{\Omega_e}$.

Linear and angular momentum balance in both the elastic solid and fluid phases on a continuum scale leads to the Cauchy momentum equation

$$\frac{\partial \mathbf{v}}{\partial t} + \nabla \cdot (\mathbf{v} \otimes \mathbf{v}) = -\frac{1}{\rho} \nabla p + \frac{1}{\rho} \nabla \cdot \boldsymbol{\sigma}', \quad \mathbf{x} \in \Sigma \quad (2.1)$$

where $t \in \mathbb{R}^+$ represents time, $\mathbf{v} : \Sigma \times \mathbb{R}^+ \mapsto \mathbb{R}^2$ represents the velocity field, ρ denotes material density, $p : \Sigma \times \mathbb{R}^+ \mapsto \mathbb{R}$ represents the hydrostatic pressure field, and $\boldsymbol{\sigma}' : \Sigma \times \mathbb{R}^+ \mapsto \mathbb{R}^2 \otimes \mathbb{R}^2$ stands for the deviatoric Cauchy stress tensor field. Throughout this work, the prime symbol $'$ on a tensor \mathbf{A} indicates its deviatoric, i.e. $\mathbf{A}' := \mathbf{A} - \frac{1}{2} \text{tr}(\mathbf{A}) \mathbf{I}$, where \mathbf{I} stands for the identity tensor and $\text{tr}(\cdot)$ represents the trace operator. All fields defined above are assumed to be sufficiently smooth in time and space. Additionally, incompressibility of the fluid and elastic domains results in the kinematic constraint on the velocity field

$$\nabla \cdot \mathbf{v} \equiv 0, \quad \mathbf{x} \in \Sigma. \quad (2.2)$$

Interactions between the fluid and elastic solid phases take place via interfacial boundary conditions, which correspond to continuity in velocities (no-slip) and traction forces at the fluid–elastic solid interface

$$\mathbf{v} = \mathbf{v}_f = \mathbf{v}_e, \quad \mathbf{n} \cdot \boldsymbol{\sigma}_f \cdot \mathbf{n} = \mathbf{n} \cdot \boldsymbol{\sigma}_e \cdot \mathbf{n}, \quad \mathbf{n} \cdot \boldsymbol{\sigma}_f \cdot \mathbf{t} = \mathbf{n} \cdot \boldsymbol{\sigma}_e \cdot \mathbf{t}, \quad \mathbf{x} \in \partial\Omega_e \quad (2.3)$$

where \mathbf{n} and \mathbf{t} denote the unit outward (solid to fluid) normal vector and the unit tangent vector at the interface $\partial\Omega_e$, respectively. Here, \mathbf{v}_f and \mathbf{v}_e correspond to the interfacial velocities in the fluid and the elastic body, respectively, while $\boldsymbol{\sigma}_f = -p\mathbf{I} + \boldsymbol{\sigma}'_f$ and $\boldsymbol{\sigma}_e = -p\mathbf{I} + \boldsymbol{\sigma}'_e$ correspond to the interfacial Cauchy stress tensor in the fluid and the elastic body, respectively.

2.2. Constitutive laws

In order to achieve closure of the above set of equations (Eqs. 2.1 to 2.3), we need to specify the form of internal material stresses, i.e. the constitutive relations. In the following, we discuss specific modeling choices for the deviatoric Cauchy stress tensor $\boldsymbol{\sigma}'$ of Eq. 2.1.

We assume the fluid to be Newtonian, isotropic and incompressible with density ρ_f , dynamic viscosity μ_f and kinematic viscosity $\nu_f = \mu_f / \rho_f$. Accordingly, the Cauchy stress is defined as follows

$$\boldsymbol{\sigma}_f' := 2\mu_f \mathbf{D}' \quad (2.4)$$

where \mathbf{D}' is the strain rate tensor $\frac{1}{2} (\nabla \mathbf{v} + \nabla \mathbf{v}^T)$.

Next, we assume that the elastic solid is isotropic, incompressible, has constant density ρ_s and exhibits *visco-elastic* behavior. Then the deviatoric Cauchy stress can be defined as

$$\boldsymbol{\sigma}'_e := 2\mu_s \mathbf{D}' + \boldsymbol{\sigma}'_{he}, \quad (2.5)$$

where μ_s represents the dynamic viscosity of the solid phase and \mathbf{D}' is the strain rate tensor. Similar to the fluid phase, the kinematic viscosity of the solid is defined as $\nu_s = \mu_s / \rho_s$.

The term $\boldsymbol{\sigma}'_{he}$ corresponds to the hyperelastic contribution to the deviatoric solid stress tensor. In this work, $\boldsymbol{\sigma}'_{he}$ is described through the generalized Mooney–Rivlin model (Bower 2009; Sugiyama *et al.* 2011), appropriate to capture elastomeric and biological tissue responses

$$\boldsymbol{\sigma}'_{he} := (2c_1 \mathbf{B} + 2c_2 (\text{tr}(\mathbf{B})\mathbf{B} - \mathbf{B} \cdot \mathbf{B}) + 4c_3 (\text{tr}(\mathbf{B}) - 2)\mathbf{B})', \quad (2.6)$$

where \mathbf{B} is the left Cauchy–Green deformation tensor $\mathbf{B} := \mathbf{F}\mathbf{F}^T$, with \mathbf{F} defined as the deformation gradient tensor $\mathbf{F} := \partial \mathbf{x} / \partial \mathbf{X}$. Here \mathbf{X} and \mathbf{x} correspond to the position of a material point at rest and after deformation, respectively.

In the infinitesimal deformations limit, the entity $2(c_1 + c_2)$ represents G , the elastic shear modulus of the solid. Finally, setting $c_2 = c_3 = 0$ and $2c_1 = G$ in Eq. 2.6, results in the deviatoric Cauchy stress of a neo-Hookean material

$$\boldsymbol{\sigma}'_{he} = G\mathbf{B}'. \quad (2.7)$$

Although the neo-Hookean model has been developed to capture non-linear stress-strain behaviours, it does so to a lesser degree of generality relative to the generalized Mooney–Rivlin model (Eq. 2.6). Nonetheless, we consider here the neo-Hookean model as well, due to its simplicity, popularity (Bower 2009; Mihai & Gorieli 2017) and for comparison.

3. Derivation of analytical solutions for neo-Hookean solids

3.1. Simplification of governing equations

We begin by noting that the problem is homogeneous in the x -direction and hence we can omit the x -dependence of any quantity. The problem then reduces to one-dimension, with gradients only along the y -axis, and classical symmetry reductions to the governing Cauchy momentum equation can be adopted. First, the continuity equation (or equivalently the incompressibility condition) of Eq. 2.2 simplifies to

$$\frac{\partial v_y}{\partial y} \equiv 0.$$

A trivial solution to this equation is $v_y(y, t) = c(t)$, where $c(t)$ is an arbitrary quantity. Because of the absence of motion of the wall in the y -direction, $c(t)$ is identically zero to match wall boundary conditions. Then, only the displacement $u(y, t)$, velocity $v(y, t)$ and stresses $\sigma_{xy} = \sigma(y, t)$ in the x direction need to be considered. This simplifies the governing equation Eq. 2.1 to read as

$$\begin{aligned} \partial_t u &= v, \\ \rho \partial_t v &= \partial_y \sigma, \end{aligned} \quad (3.1)$$

where all quantities depend on (y, t) . Additionally, the stress can be directly computed from Eqs. (2.4) to (2.6) as follows

$$\sigma = \begin{cases} \mu_f \partial_y v & \text{for fluid } (L_s \leq |y| < L_s + L_f) \\ 2c_1 \partial_y u + 4c_3 (\partial_y u)^3 + \mu_s \partial_y v & \text{for solid } (0 \leq |y| < L_s) \end{cases} \quad (3.2)$$

where we remark that the coefficient c_2 from Eq. 2.6 drops out due to algebraic simplification and hence does not contribute to the dynamics. We also note that $c_3 = 0$ implies linear stress responses with respect to the 1D displacement u , while $c_3 \neq 0$ is responsible for (cubic) nonlinear behaviors (Sugiyama *et al.* 2011). The simplified Eqs. (3.1) and (3.2) indicate that accelerations (LHS) result from viscous forces in the fluid, and a combination of viscous and elastic forces in the solid (RHS).

Further, velocities and stresses at the interfaces need to be continuous per Eq. 2.3, thus

$$\begin{aligned} v(\pm L_s^+, t) &= v(\pm L_s^-, t) \\ \mu_f \partial_y v(\pm L_s, t) &= 2c_1 \partial_y u(\pm L_s, t) + 4c_3 (\partial_y u(\pm L_s, t))^3 + \mu_s \partial_y v(\pm L_s, t). \end{aligned} \quad (3.3)$$

Finally, we close the equations above by imposing no-slip boundary conditions at the upper and lower walls at $y = \pm(L_s + L_f)$

$$v = \begin{cases} \hat{V}_{\text{wall}} \sin \omega t & \text{at } y = L_f + L_s \\ -\hat{V}_{\text{wall}} \sin \omega t & \text{at } y = -(L_f + L_s). \end{cases} \quad (3.4)$$

In the case of a neo-Hookean constitutive model ($c_3 = 0$), the governing equations Eqs. (3.1) to (3.3) reduce to a set of linear equations since our setup involves purely shearing motions. We take two distinct, but equivalent, solution approaches. The first one involves directly solving the linear governing equations in the physical domain. The second one instead solves the modal form of the governing equations obtained via a sine transform. The first solution is elegant and compact, but only possible in the neo-Hookean case, while the second solution is convoluted, but can handle arbitrary constitutive models. We discuss both in the following.

3.2. Direct analytical solution

We first directly solve Eqs. (3.1) and (3.2) in the fluid and solid domain. Given $c_3 = 0$, we have

$$\begin{aligned} \rho_f \partial_t v_f &= \mu_f \partial_y^2 v_f & \text{for fluid } (L_s \leq y < L_s + L_f) \\ \rho_s \partial_t^2 u_s &= 2c_1 \partial_y^2 u_s + \mu_s \partial_y^2 \partial_t u_s & \text{for solid } (0 \leq y < L_s). \end{aligned} \quad (3.5)$$

Considering the linearity of Eq. 3.5, symmetry of our setup, and the sinusoidal form of wall velocity $V_{\text{wall}}(t) = \text{Im} [\hat{V}_{\text{wall}} \exp(i\omega t)]$, one can expect similar sinusoidal forms in resulting displacements $u_s(y, t) = \text{Im} [\hat{u}(y) \exp(i\omega t)]$ and velocities $v_f(y, t) = \text{Im} [\hat{v}(y) \exp(i\omega t)]$. Substituting these ansatzes in Eq. 3.5 yields

$$\begin{aligned} \left(\partial_y^2 - \frac{i\omega}{\nu_f} \right) \hat{v}_f &= 0 & \text{for fluid } (L_s \leq y < L_s + L_f) \\ \left(\partial_y^2 + \frac{\omega^2}{i\omega\nu_s + (2c_1/\rho_s)} \right) \hat{u}_s &= 0 & \text{for solid } (0 \leq y < L_s) \end{aligned} \quad (3.6)$$

which are a pair of homogeneous Helmholtz equations with exact solutions

$$\begin{aligned} \hat{v}_f(\tilde{y}) &= A \exp\left(k_f \frac{\tilde{y}}{L_f}\right) + B \exp\left(-k_f \frac{\tilde{y}}{L_f}\right) & \tilde{y} \in [0, L_f) \\ \hat{u}_s(y) &= C \exp\left(k_s \frac{y}{L_s}\right) + D \exp\left(-k_s \frac{y}{L_s}\right) & y \in [0, L_s), \end{aligned} \quad (3.7)$$

where

$$k_f = \sqrt{i} \left(L_f^{-1} (\nu_f / \omega)^{0.5} \right)^{-1}, \quad k_s = i \left[\left((\omega L_s)^{-1} (2c_1 / \rho_s)^{0.5} \right)^2 + i \left(L_s^{-1} (\nu_s / \omega)^{0.5} \right)^2 \right]^{-0.5}. \quad (3.8)$$

The coefficients A, B, C, D are directly determined given interface and boundary conditions (Eqs. 3.3, 3.4), and their expressions are reported in Supplementary Information ???. Physically, Eq. 3.7 indicates a wave-like behavior, coupled with exponential decay, in both solid and fluid domains.

3.3. Modal solutions using Fourier series

In the second approach, the solution strategy is to represent $u(y, t)$, $v(y, t)$ as a Fourier sine series in the spatial coordinate y , inject it into the governing equations 3.1, 3.2, and match the interfacial conditions of Eq. 3.3 and boundary conditions of Eq. 3.4 to obtain closed-form solutions. The choice of a sine series expansion is natural here given the Dirichlet velocity boundary conditions. Because of the piecewise definition of stresses in Eq. 3.2 and interfacial condition in Eq. 3.3 (which indicates that velocities are C^0 continuous), convergence can be poor if a global Fourier series (i.e. for both the solid and fluid domains together) is considered. Hence, we utilize two piecewise Fourier series expansions for the solid $v_s(y, t)$ and fluid $v_f(y, t)$ velocities, respectively, and explicitly impose C^0 continuity in velocities and stresses.

We begin by noting that due to symmetry, Eq. 3.1 can only admit solutions which are odd functions of y . Indeed, the equations of motion are invariant upon replacing $u(y, t)$, $v(y, t)$ with $-u(-y, t)$, $-v(-y, t)$. Then, one can expand $u(y, t)$, $v(y, t)$ using the Fourier sine series only in the upper half space $y \geq 0$, as follows

$$\begin{aligned} v_f(\tilde{y}, t) &= V_I(t) + \frac{\tilde{y}}{L_f} (V_{\text{wall}}(t) - V_I(t)) + \sum_{k=1}^{\infty} v_{f,k}(t) \sin \frac{\pi k \tilde{y}}{L_f} \\ u_s(y, t) &= \frac{U_I(t)y}{L_s} + \sum_{k=1}^{\infty} u_{s,k}(t) \sin \frac{\pi k y}{L_s} \end{aligned} \quad (3.9)$$

where $U_I(t)$, $V_I(t)$ is the displacement and velocity of the solid–fluid interface at $y = L_s$, $\tilde{y} = y - L_s$, and $v_{f,k}(t)$ and $u_{s,k}(t)$ are the Fourier expansion coefficients of v_f and u_s , respectively. This expansion satisfies the incompressibility condition (Eq. 2.2), odd symmetry requirement about $y = 0$, interfacial velocity conditions (Eq. 3.3), and boundary velocity conditions (Eq. 3.4) imposed in the setup. Additional details regarding the expansion can be found in Supplementary Information ???. We also note that the interface displacement U_I and modal displacement $u_{s,k}$ satisfy

$$\frac{dU_I}{dt} = V_I, \quad \frac{du_{s,k}}{dt} = v_{s,k}. \quad (3.10)$$

Substituting the Fourier-series defined in Eq. 3.9 into the governing Eq. 3.1 and utilizing the stress relations of Eq. 3.2, we rewrite the equations with all terms moved to the LHS

$$\begin{aligned} \frac{dV_I}{dt} + \frac{\tilde{y}}{L_f} \left(\frac{dV_{\text{wall}}}{dt} - \frac{dV_I}{dt} \right) + \sum_{k=1}^{\infty} \left\{ \frac{dv_{f,k}}{dt} + v_f \left(\frac{\pi k}{L_f} \right)^2 v_{f,k} \right\} \sin \frac{\pi k \tilde{y}}{L_f} &= 0 \\ \frac{y}{L_s} \frac{dV_I}{dt} + \sum_{k=1}^{\infty} \left\{ \frac{d^2 u_{s,k}}{dt^2} + v_s \left(\frac{\pi k}{L_s} \right)^2 \frac{du_{s,k}}{dt} + \frac{2c_1}{\rho_s} \left(\frac{\pi k}{L_s} \right)^2 u_{s,k} + \frac{\pi k}{\rho_s L_s} \sigma_{\text{NL},k} \right\} \sin \frac{\pi k y}{L_s} &= 0 \end{aligned} \quad (3.11)$$

where $v_s = \mu_s / \rho_s$ and $v_f = \mu_f / \rho_f$ are the kinematic viscosities of the solid and fluid phases, respectively. Here, σ_{NL} denotes the nonlinear contribution (i.e. the term containing c_3) in the

solid stress Eq. 3.2 with respect to the displacement, so that its expansion coefficients read

$$\sigma_{\text{NL}} := 4c_3 \left(\frac{\partial u_s}{\partial y} \right)^3 = \sum_{k=0}^{\infty} \sigma_{\text{NL},k} \cos \frac{\pi k y}{L_s}. \quad (3.12)$$

We now project the governing equations in physical space (Eq. 3.11) onto the Fourier modal bases, and then use Fourier identities (Supplementary Information ??) to simplify the obtained expressions

$$\frac{2}{\pi k} \left\{ \frac{dV_I}{dt} - (-1)^k \frac{dV_{\text{wall}}}{dt} \right\} + \frac{dv_{f,k}}{dt} + v_f \left(\frac{\pi k}{L_f} \right)^2 v_{f,k} = 0 \quad (3.13)$$

$$- \frac{2(-1)^k}{\pi k} \frac{dV_I}{dt} + \frac{d^2 u_{s,k}}{dt^2} + v_s \left(\frac{\pi k}{L_s} \right)^2 \frac{du_{s,k}}{dt} + \frac{2c_1}{\rho_s} \left(\frac{\pi k}{L_s} \right)^2 u_{s,k} + \frac{\pi k}{\rho_s L_s} \sigma_{\text{NL},k} = 0 \quad (3.14)$$

with $k = 1, \dots, \infty$. In modal space, the continuity condition of shear stresses at the interface, upon substituting Eq. 3.9 into Eq. 3.3 and using the Fourier identities of Supplementary Information ??, reads

$$\begin{aligned} & \frac{\mu_f (V_{\text{wall}} - V_I)}{L_f} - \frac{2c_1 U_I}{L_s} - \sigma_{\text{NL},0} \\ & - \frac{\mu_s V_I}{L_s} \sum_{k=1}^{\infty} \left[\frac{\mu_f \pi k v_{f,k}}{L_f} - (-1)^k \left\{ \frac{2c_1 \pi k u_{s,k}}{L_s} + \frac{\mu_s \pi k}{L_s} \frac{du_{s,k}}{dt} + \sigma_{\text{NL},k} \right\} \right] = 0. \end{aligned} \quad (3.15)$$

Equations (3.13) to (3.15) directly relate the modal expansion coefficients $v_{f,k}$ in the fluid, and $u_{s,k}$ in the solid, via the interfacial quantities U_I, V_I as a function of the physical setup parameters. We now need to solve Eq. 3.13 to Eq. 3.15 for the modal quantities $v_{f,k}, u_{s,k}$ and interfacial quantities U_I, V_I . To do so, we truncate the number of modes in the above infinite Fourier series to $k = K - 1$. This leads to a truncation error, which we minimize by taking K to be large. Here, K is fixed to 1024 unless otherwise indicated.

We now specialize the above solutions for the neo-Hookean case with $c_3 = 0$. First, similar to Section 3.2, we expect sinusoidal forms for the temporal quantities

$$V_I(t) = \text{Im} [\hat{V}_I \exp(i\omega t)], \quad v_{f,k}(t) = \text{Im} [\hat{v}_{f,k} \exp(i\omega t)], \quad u_{s,k}(t) = \text{Im} [\hat{u}_{s,k} \exp(i\omega t)]. \quad (3.16)$$

Substitution of the temporal transformed quantities from Eq. 3.16 in the momentum ODEs (Eqs. 3.13, 3.14) leads to algebraic equations that can be solved. Upon algebraic manipulation and taking into account the modal stress balance (Eq. 3.15), we obtain

$$\hat{u}_{s,k} = -\frac{i(-1)^k \hat{V}_I \beta_k}{\pi \omega k}, \quad \hat{v}_{f,k} = \frac{\{(-1)^k \hat{V}_{\text{wall}} - \hat{V}_I\} \alpha_k}{\pi k} \quad (3.17)$$

where $\hat{V}_I, \alpha_k, \beta_k$ are coefficients whose expressions are tedious and hence deferred to Supplementary Information ??. The expressions of Eq. 3.17 can then be directly used in Eq. 3.9 to analytically evaluate solid displacements, fluid velocities and solid velocities. This provides the final modal solution for the case of a neo-Hookean solid.

Our solution approaches are equivalent and generate the same results (Supplementary Information ??). Having discussed both these approaches, we now identify key non-dimensional quantities that physically characterize the system, validate our solutions against known special cases and direct numerical simulations, analyze parametric behavior and investigate implications on the system response.

| Symbol | Definition | Physical interpretation |
|----------------|--|---|
| L | $2(L_s + L_f)$ | Length scale |
| L_f/L_s | | Length ratio |
| $\dot{\gamma}$ | $2\hat{V}_{\text{wall}}/\omega L$ | Non-dimensional shear rate |
| Re | $\dot{\gamma}\omega L_f^2/\nu_f$ | Reynolds number |
| Er | $\mu_f \dot{\gamma}\omega/2c_1$ | Ericksen number |
| ρ | ρ_s/ρ_f | Density ratio |
| ν | ν_s/ν_f | Viscosity ratio |
| δ_f | $L_f^{-1} (\nu_f/\omega)^{0.5} = \exp(i\pi/4) k_f^{-1} = \left(\frac{\dot{\gamma}}{Re}\right)^{0.5}$ | Non-dimensional fluid Stokes layer thickness |
| δ_s | $L_s^{-1} (\nu_s/\omega)^{0.5} = \sqrt{\text{Im}[-k_s^{-2}]} = (L_f/L_s) \left(\frac{\nu\dot{\gamma}}{Re}\right)^{0.5}$ | Non-dimensional solid Stokes layer thickness |
| λ | $(\omega L_s)^{-1} (2c_1/\rho_s)^{0.5} = \sqrt{\text{Re}[-k_s^{-2}]} = (L_f/L_s) \left(\frac{\dot{\gamma}^2}{\rho Re Er}\right)^{0.5}$ | Non-dimensional elastic wavelength |

Table 1: Characteristic non-dimensional parameters

4. Analysis of system behavior for neo-Hookean solids

4.1. Key driving parameters

The proposed system can be fully characterized through a set of non-dimensional parameters, deduced from our solutions above, which are listed in Table 1. Here the Reynolds number Re captures the importance of inertial effects in the fluid phase using the ratio of inertial to viscous forces. Higher Re indicates an inertia-dominated response from the fluid. The Ericksen number Er captures the importance of elasticity in the solid phase using the ratio of viscous to elastic forces. Lower Er indicates an elasticity-dominated response from the solid. The fluid Stokes-layer thickness δ_f captures the boundary layer length scale associated with the exponential decay of wall velocity, relative to the fluid layer thickness. Low values of δ_f indicate significant decay of wall velocity before reaching the interface. The solid Stokes-layer thickness δ_s has a similar interpretation, but for the solid layer. The elastic wavelength λ captures the length scale associated with elastic shear waves progressing from the interface into the solid bulk, relative to the solid layer thickness. Low values of λ indicate high number of elastic-waves within the solid phase. The relevance of these length scales $\delta_f, \delta_s, \lambda$ will become apparent as we discuss the system response in Section 4.2.

In this work, we fix the geometry $L_s = L_f = L/4$, and unless stated otherwise, we assume non-dimensional shear rate $\dot{\gamma} = \pi^{-1}$ and density ratio $\rho = 1$. We remark that these assumptions do not affect the generality of our results. Indeed, the effects of $\dot{\gamma}, \rho$ can be reproduced through fluid viscosity ν and solid elasticity c_1 , via the non-dimensional parameters of Table 1.

Having defined the key non-dimensional parameters, we can now investigate their impact on the behavior of the system.

4.2. Limit cases

In order to develop a physical intuition for the system response, we first selectively remove the effects of solid viscosity ($\nu_s \rightarrow 0$) and elasticity ($c_1 \rightarrow 0$) and analyze our solution. In these limit cases we recover classical analytical results.

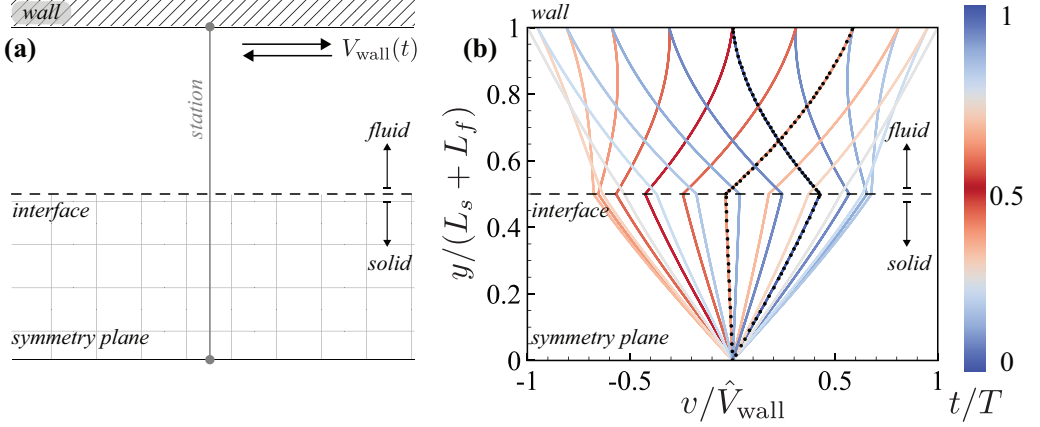


Figure 2: Pure elastic solid limit. Non-dimensional velocity profiles in y for a pure elastic solid with a neo-Hookean constitutive model. The system response is shown only in the upper half plane. The system is characterized by $Re = 0.25$, $Er = 1/(5\pi)$, $\nu = 0$, $\delta_f = 1.12$, $\delta_s = 0$, $\lambda = 2.52$. Additional details can be found in Supplementary Information ???. The same set of parameters are analyzed in Sugiyama *et al.* (2011), whose profiles (only provided at two time instants) are overlaid as black scatter points on our curves. Colors represent t/T .

4.2.1. Purely elastic solid case ($\nu_s = 0$)

In the limit of $\nu_s = 0$, the solid is purely elastic and we recover the solution of Sugiyama *et al.* (2011) (up to minor typographical errors in that work). Here we consider the setup shown in Fig. 2 with parameters taken from Sugiyama *et al.* (2011), to enable comparison with their results. This system is characterized by $Re = 0.25$, $Er = 1/(5\pi)$, $\nu = 0$, $\delta_f = 1.12$, $\delta_s = 0$, $\lambda = 2.52$.

We begin our comparison by highlighting typical non-dimensional velocity profiles obtained from our solutions. We only showcase profiles in the upper half-plane, shown in Fig. 2a, due to symmetry in our setup. We plot the profiles corresponding to the marked line station in Fig. 2a, at different time instants (or equivalently phases) within one oscillation cycle. These profiles are presented in Fig. 2b, with colors indicating time instants. For reference, the wall is located at $y/(L_s + L_f) = 1$ and the symmetry plane is located at $y/(L_s + L_f) = 0$. The interface is located at $y/(L_s + L_f) = 0.5$, below which we have the elastic solid zone and above which we have the fluid zone. In this plot we also overlay the velocity profiles (black points) predicted by Sugiyama *et al.* (2010). While they provide profile data for only two time instants, we find favorable agreement with our velocity profiles, at both these times. From these velocity profiles, we see that the solid velocity exhibits a phase lag (indicated by the colors) relative to the fluid velocity, and less pronounced magnitudes. The fluid's maximal velocity magnitude always occurs at the wall ($|v| = \hat{V}_{\text{wall}}$) while the solid velocity magnitudes always reach a minimum at the symmetry plane ($|v| = 0$). Finally, the slopes of the velocity profiles $\partial_y v$ are discontinuous at the interface, to satisfy continuity in stresses (Eq. 3.3).

We can gain an intuition for these profiles by considering force balance in the fluid and solid phases separately. That is, at any point in space-time, the sum of all real and apparent (i.e. inertial acceleration) forces must add up to zero. In the viscous fluid, we have inertial and viscous contributions, as seen from $-\partial_t v + \nu \partial_y^2 v = 0$. This balance equation indicates that viscous forces operate by acting on the curvature $\partial_y^2 v$ of the velocity profile. Thus, both high viscosity ν (low Re) and high velocity profile curvature $\partial_y^2 v$ contribute to increasing

viscous forces, which then exactly balance out accelerations. Typically, these viscous forces (and velocity profile curvatures) are concentrated within a boundary layer close to the wall (seen from the structure of the solution in Eq. 3.7), characterized by the non-dimensional Stokes layer thickness δ_f . Within this boundary layer, viscous forces cause the flow velocity to rapidly decay before eventually reaching the interface.

From the moving interface (no-slip), the solid phase displacement propagates into the bulk, mediated by elastic forces. From Eqs. (3.1) and (3.2), the elastic contribution to solid force balance is $-\partial_t v + 2c_1 \partial_y^2 u = 0$. This indicates that elastic forces operate by acting on the curvature $\partial_y^2 u \propto \omega^{-1} \partial_y^2 v$ of the solid velocity profile v . So both high elastic shear modulus $2c_1$ (low Er) and high velocity profile curvature $\partial_y^2 v$ contribute to increasing elastic forces. These elastic forces propagate as waves within the solid ($\nu_s = 0$, so λ_2 from Eq. 3.8 is purely imaginary, leading to sinusoids in Eq. 3.7), characterized by the non-dimensional elastic wavelength λ . This implies that a wave profile can be expected for velocities (and curvatures) within the solid, which then always adjusts to zero at the symmetry plane in a fashion similar to *nodes* in stationary waves. Additionally, for a viscoelastic solid ($\nu_s \neq 0$), we have viscous effects that set up a boundary layer close to the interface and symmetry planes, similar to the fluid phase. The extent of this region is characterized by the non-dimensional solid Stokes layer thickness δ_s .

Overall, across both fluid and solid phases, we can rationalize the observed velocity profiles by considering Re , Er and the curvature length scales δ_f , δ_s , λ . Referring back to Fig. 2, since $Re = 0.25 \sim O(1)$, we expect inertial and viscous forces to be approximately equally important in the fluid. Additionally, $\delta_f = 1.12 > 1$ indicates that the boundary layer occupies most of the fluid zone. This leads to moderate velocity curvatures throughout the fluid phase, as seen in Fig. 2b. This, in turn, drives the solid phase characterized by no viscosity and low Er , indicating stiff/strong elastic behavior. As a consequence of low Er , the wavelength $\lambda \propto Er^{-0.5}$ is large ($\lambda = 2.52 > 1$). We then expect to see only the nascent part of a wave, which is almost linear, as indeed observed in Fig. 2b.

4.2.2. No elastic solid ($c_1 = 0$): single phase and multi-phase Stokes–Couette flows

Our solution recovers classical results in the limit of $c_1 = 0$, which indicates absence of elastic forces in the solid phase. Thus, only viscous forces operate in the solid, effectively rendering it a Newtonian fluid. If $c_1 = 0$, $\mu_s = \mu_f = \mu$, and $\rho_s = \rho_f = \rho$, then the entire domain is occupied by a single fluid, and we recover the Stokes–Couette flow solution (Landau & Lifshitz 1987) valid throughout the domain. If instead $c_1 = 0$ but now $\mu_s \neq \mu_f$ or $\rho_s \neq \rho_f$, then the domain is occupied by two different fluids, and we recover the multi-phase Stokes–Couette flow for two immiscible liquids, which has established piecewise analytical solutions (Sim 2006; Leclaire *et al.* 2014). Upon comparison with single- and double-phase reference Stokes–Couette flow solutions, our analytical formulations (Sections 3.2 and 3.3) are found in excellent agreement (Supplementary Information ??).

4.3. Neo-Hookean solid: Verification against numerical simulations

We now move on from analyses of limit cases and consider the more general scenario of visco-hyperelastic Neo-Hookean solids. Before studying the system behavior in a range of conditions (Section 4.4), we validate our solutions against direct numerical simulations employing a recent two-dimensional remeshed-vortex method framework (Bhosale *et al.* 2021). In Fig. 3a, we consider a system characterized by $Re = 2$, $Er = 1$, $\nu = 0.1$, $\delta_f = 0.4$, $\delta_s = 0.126$, $\lambda = 0.225$. In these conditions $Re, Er \sim O(1)$ so that we expect elastic, viscous and inertial forces to be equally important in the solid, marking a departure from the

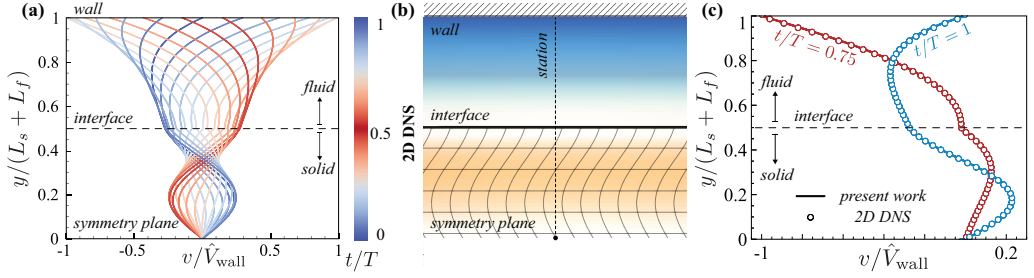


Figure 3: Comparison against simulations. (a) Non-dimensional analytical velocity profiles in y , for a visco-elastic solid with a neo-Hookean constitutive model. The system response is shown only in the upper half plane. This system is characterized by $Re = 2$, $Er = 1$, $\nu = 0.1$, $\delta_f = 0.4$, $\delta_s = 0.126$, $\lambda = 0.225$. Additional details can be found in Supplementary Information ?? . Colors indicate t/T . (b) We solve the above problem through 2D DNS (Bhosale *et al.* 2021) and run our simulations until the system reaches dynamical steady state ($t/T = 10$), and then sample quantities within the last cycle. Corresponding simulation parameters are found in Supplementary Information ?? . In the image, we mark the x -velocity field (orange/blue represent positive/negative velocity) and deformation contours within the solid, with the interface marked (black, thick solid) for visual clarity. (c) Upon plotting the velocity profiles at the highlighted station (black, dashed) in the center of the domain, we see good agreement with our analytical results across all times. For the sake of clarity, we only show profiles at two different time instances. Here numerical results are plotted with scatter points whereas analytical results are plotted with a solid line.

above limit cases. Additionally, since $\lambda < 1$, we expect the emergence of wave-like profiles inside the solid. As illustrated in Fig. 3a, our analytical solutions within the solid indeed exhibit a standing wave-like behavior, constrained by boundary layer adjustments (with characteristic high curvatures) both near the interface and the symmetry plane. Further, these results are confirmed by our direct simulations as illustrated in Fig. 3c, where we report the numerically obtained velocity profiles along the line-station of Fig. 3b, overlaid on the theoretical predictions. As can be seen, profiles compare favorably at multiple temporal instants, validating the accuracy of both our theory and numerical solver.

4.4. Range of soft, elastomeric interface dynamics

Having validated our analytical solutions across different scenarios, we next investigate the dynamic response of the system for variations in the two most important parameters: elasticity (Er) and viscosity (Re). Here we span the set of $Er = [0.1, 1, 10]$, which includes the range of soft cellular tissue found in the human body (Wu *et al.* 2018; Guimarães *et al.* 2020) and $Re = [0.1, 0.5, 1, 2, 10]$, which indicates small to moderate inertial effects. Our choices capture typical values found in oscillatory micro-fluidic assays and applications involving biological and soft elastomeric materials that operate in conjunction with fluid interfaces (Di Carlo 2009; Velve-Casquillas *et al.* 2010; Duncombe *et al.* 2015).

Of further relevance in the context of our minimal setup, we also find in-situ studies of bacterial deposition on coated, elastic surfaces in pulsatile flows (Bakker *et al.* 2003). In these cases, preferential adhesion based on elastic stiffness has been reported (Song *et al.* 2015), offering avenues to modulate bio-film formation and preventing bio-fouling. Our model may offer insights for the manipulation of oscillatory flow-stresses through soft elastic coatings (Gad-el Hak 2002). Another potential application connects to the mechanics and wear of loaded human synovial joints (Dowson & Jin 1986; Sun *et al.* 2003; Nalim *et al.* 2004; Sun 2010), where wall-driven, cyclic (synovial) fluid shear stresses act on soft articular

cartilages. Finally, our model may be of use in non-destructive testing of solid rheological properties, similar to Couette visco- and elasto-meters (Carr *et al.* 1976).

Within this context, we focus on the system response (velocity profiles) first at low $Re = 0.1$ (top row of Fig. 4), then at (relatively) high $Re = 10$ (bottom row) and finally at intermediate Re (middle rows). For each Re , we consider the impact of Er , ranging from stiff (low Er , left column) to soft solids (high Er , right column). Within each Re regime, we discuss the fluid velocity profiles first, followed by the solid velocity profiles. Velocity profiles are rationalized using the length scales $\delta_f = (\dot{\gamma} Re)^{-0.5}$, $\delta_s = (\nu \dot{\gamma} / Re)^{0.5}$ and $\lambda = \dot{\gamma} (Re Er)^{-0.5}$, which are marked alongside each case study.

4.4.1. Low Re

First, at low $Re = 0.1$, we expect viscous forces to be important in the bulk flow. Indeed, the boundary layer in the fluid zone is characterized by $\delta_f \approx 1.8 > 1$, so that its thickness spans the entire flow domain. This thick boundary layer results in two prominent effects. First, it indicates that fluid velocities have minimal curvature, which we confirm from the top row of Fig. 4. Additionally, it effectively transmits the viscous stresses induced by the wall to the interface, which then initiates motion in the bulk solid. At this low Re , the thickness $\delta_s \approx 0.6$ of the solid boundary layer spans the bulk of the solid domain itself. In addition, unlike the fluid phase, we now also have elastic contributions, which we investigate by spanning Er . At low $Er = 0.1$, the solid has a large elastic wavelength $\lambda \approx 3.2 > 1$. Hence, similar to Section 4.2.1, we expect the velocity profiles to have no wave-like behavior, and thus less curvature. This is confirmed by the left column of Fig. 4, where we see approximately linear solid velocity profiles, intuitively justified by the fact that to balance out acceleration forces, the elasticity modulus c_1 has to be large when curvatures are minimal (see Section 4.2.1).

If we then increase Er , going from stiffer (left column) to softer solids (right column), we expect both elastic and viscous forces to equally contribute to the dynamics. This is accompanied by decreasing values of λ which indicate that more wavelengths can now fit in the solid layer thickness. Then, similar to Section 4.3, we expect the appearance of standing wave-like profiles, with prominent boundary-layer adjustments close to interface and symmetry planes. These considerations are confirmed in Fig. 4, where we see that solid velocity profiles exhibit increasing curvatures as we move from left to right in the top row.

4.4.2. Higher Re

Next, for $Re = 10$, we see prominent boundary layer adjustments in the fluid close to the wall. This is due to the characteristically low boundary layer thickness $\delta_f \approx 0.2 < 1$, which implies that fluid velocity curvatures can be high only within this compact region. Indeed, beyond this boundary layer, the fluid velocity decays rapidly before reaching the interface, leading to the profiles shown in the bottom row of Fig. 4. As a result of this decay, the flow cannot effectively transmit viscous stresses to the interface and hence the solid barely deforms. This flow decay is dependent only on Re , and so we expect similar small solid deformation amplitudes even if we vary the solid elasticity. We confirm this intuition by increasing Er (left to right), noticing small solid velocity amplitudes. Hence, in this Re regime, the fluid evolves almost independently (“weak coupling”) from the details of the solid. In contrast, the low Re regime seen earlier is “strongly coupled”. Finally, we note that increasing Er , i.e. decreasing λ , leads to wavy profiles (although of small magnitude) inside the solid.

4.4.3. Intermediate Re

For intermediate Re , the system showcases a rich variety of behaviors, which we highlight by investigating parameters around $Re = 1$. Firstly, in these cases the fluid’s boundary layer has

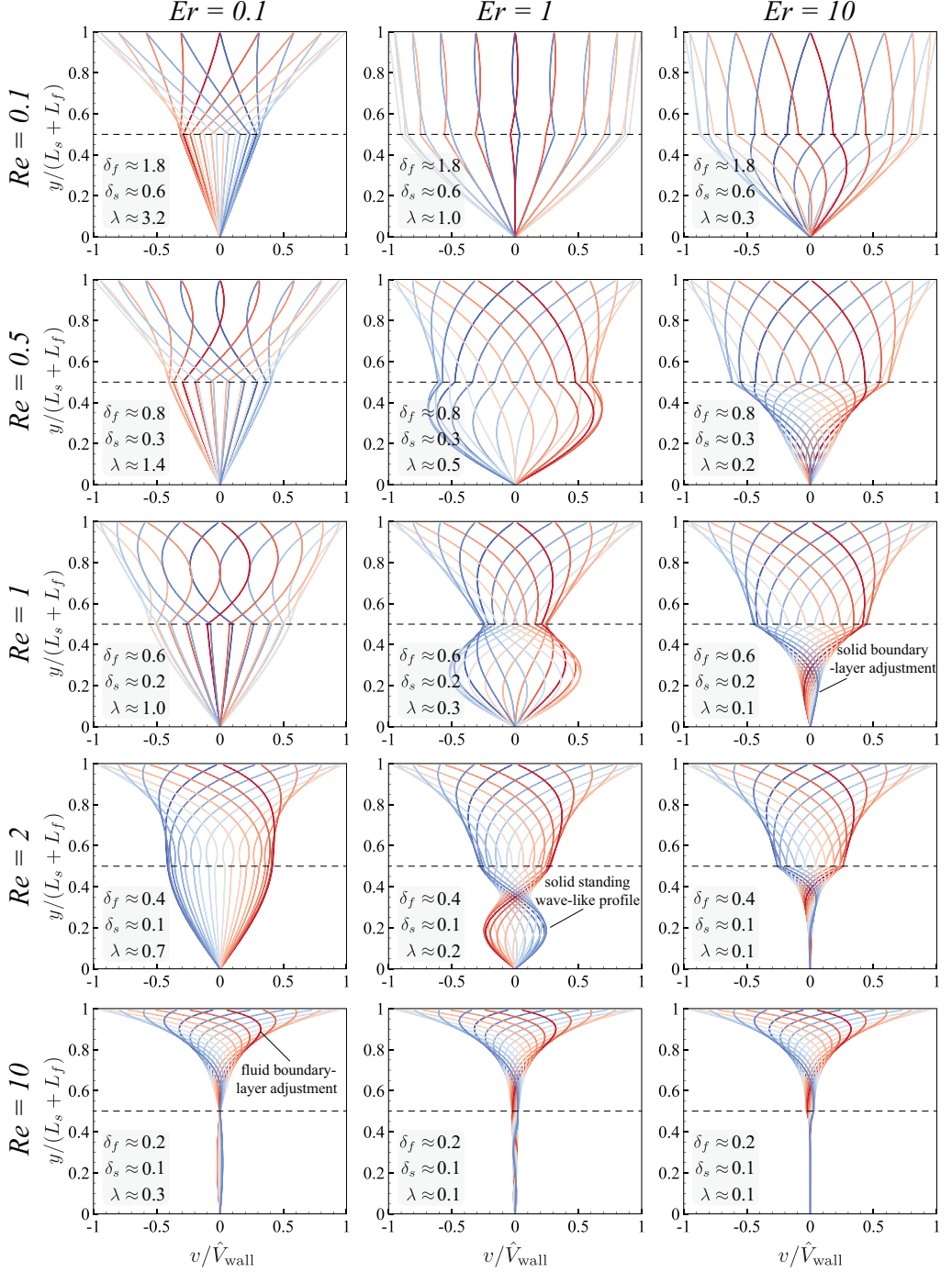


Figure 4: Dynamics with parametric variation. Non-dimensional velocity profiles in y for parametric changes in $Re = [0.1, 0.5, 1, 2, 10] \times Er = [0.1, 1, 10]$ with $\nu = 0.1, \rho = 1$.

The system response is shown only for the upper half plane, where we also mark the length scales $\delta_f, \delta_s, \lambda$. The black, dashed lines indicate the solid-fluid interface. Colors represent t/T , with the same colorbar as Fig. 2.

moderate thickness $\delta_f \sim O(1)$ and hence we expect moderate velocity profile curvatures over δ_f . By decreasing δ_f (e.g. by increasing Re), we expect the flow curvature to increase. We confirm this in Fig. 4, as we move from $Re = 0.5$ (top) to $Re = 2$ (bottom). An increase in Re also increases the solid velocity curvatures, by decreasing both the solid wavelength λ and solid boundary layer thickness $\delta_s \sim O(0.1)$. The effect of decreasing λ is prominently displayed as we move from $Re = 0.5 \rightarrow 2$ for a fixed $Er = 1$ (central column). Further, at high Er , we expect viscous forces to dominate over elastic forces, thus rendering the solid medium more fluid-like. Indeed, for $Er = 10$, the solid velocity profiles showcase a boundary-layer adjustment similar to the one encountered in fluids. Hence, as we span Er from 0.1 to 10 at intermediate $Re = 0.5 - 2$, the effects of viscosity and elasticity compete in the solid leading to rich dynamics. As a consequence, in this regime, solid velocity profiles are especially sensitive to changes in Er . Such sensitivity provides a potential mechanism to manipulate and control interfacial stress magnitudes in the previously mentioned applications. Finally, because of its dynamic variety and sensitivity, this intermediate parameter regime is identified as numerically challenging, and therefore we propose the parameter set $Re = \{0.5, 1, 2\}$ and $Er = \{0.1, 1, 10\}$ for benchmarking flow–structure interaction solvers, as illustrated in Fig. 3.

4.5. Solid phase resonance

We conclude this section by investigating the conditions under which resonant solid deformations occur. These may serve well for applications such as elastometry, where high amplitude peaks provide unique footprints to characterize materials.

We begin by defining the gain function $|G| \geq 0$ as the ratio of solid to wall amplitude which, from Eq. 3.7, takes the closed-form expression

$$|G| = \left| \frac{i\omega C}{\hat{V}_{\text{wall}}} \right| = \frac{2}{\left| \left(e^{k_f - k_s} - e^{-(k_f - k_s)} \right) (1 - \alpha) - \left(e^{k_f + k_s} - e^{-(k_f + k_s)} \right) (1 + \alpha) \right|} \quad (4.1)$$

where k_f and k_s are the fluid and solid wave contributions (Eq. 3.8), and $\alpha = \frac{L_f}{L_s} \frac{k_s}{k_f} \left(\rho\nu - i \frac{\dot{\gamma}}{Er} \right)$ captures the degree of fluid–solid coupling.

In the limit case of a purely elastic solid ($\nu = 0$) the denominator of G is always > 0 , due to the non-zero contributions from the fluid phase ($k_f \neq 0$). The immediate implication is that unbounded resonance $|G| \rightarrow \infty$, is not possible in our setup because the fluid always dampens out high amplitudes in the solid phase. Thus, interstitial fluids, beside providing lubrication as in synovial joints, may also prevent excessive deformations and subsequent failure of the soft, articular cartilage.

In Fig. 5a, we plot $|G|$ as a function of Er, Re with $\nu = 0$. As can be seen, characteristic gain peaks ($|G| > 1$, bright yellow) take place and manifest as families of hyperbolae $Re \cdot Er = k^2$. Here $k = \frac{\pi}{\lambda}$ corresponds to discrete harmonic wavenumbers with wavelength $\lambda = (\pi^2 Re Er)^{-0.5}$, from Table 1. Hence, higher k corresponds to higher harmonics. To further gain intuition, we fix $Re = 1$ (chosen because of its dynamic richness, see Fig. 4), and plot $|G|$ versus Er to obtain the red curve of Fig. 5c. We see four distinct high-gain peaks ① – ③ of increasing amplitude, where the numbers represent the standing wave mode. In the cases ① – ③, the solid displaces more than the driving wall (Fig. 5d–f), with velocity profiles corresponding to the first three harmonics. Case ① is characterized by the fact that maximal amplitudes occur at the interface, and not in the bulk, thus behaving as a standing wave with a free end at the interface.

Realistic materials include internal dissipation effects, which we enable here by adding viscosity to the solid. This drastically reduces $|G|$ amplitudes, but preserves the hyperbolic structure of peaks, as seen in Fig. 5b.

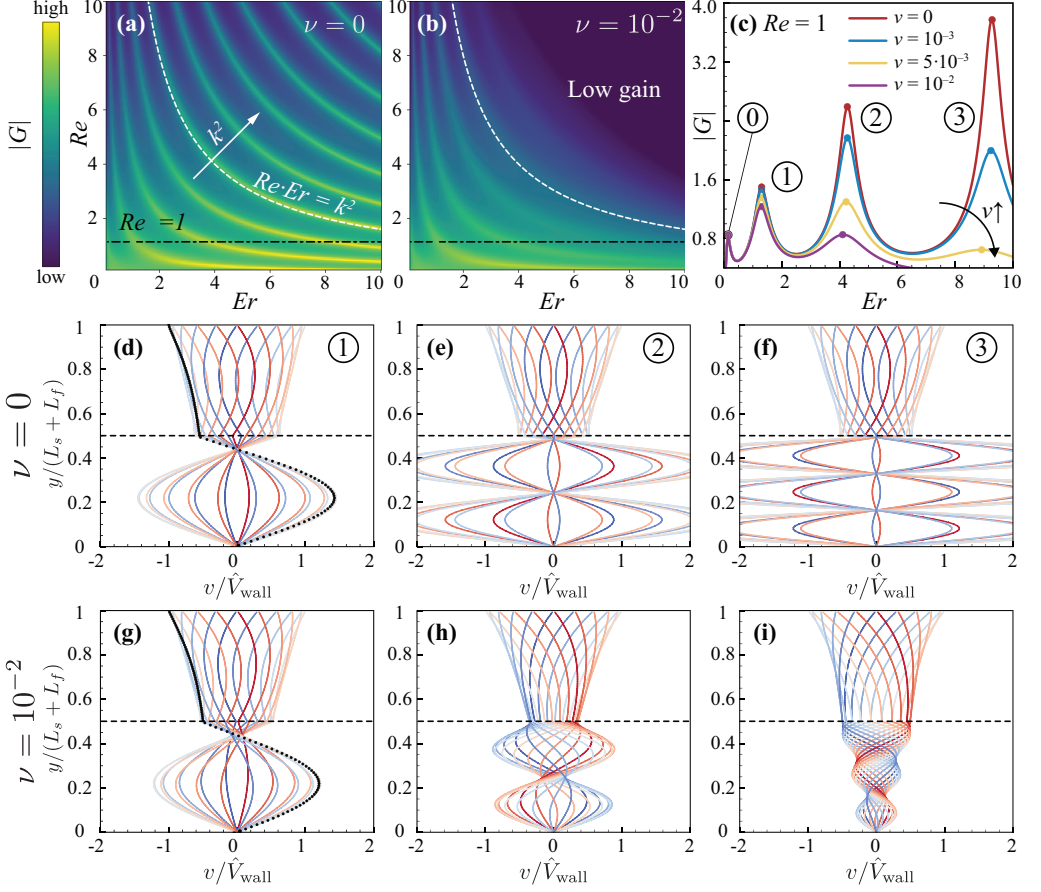


Figure 5: High amplitude gains. Phase map of $|G|$ as a function of Re , Er shows distinct regions of high (bright yellow) and low (dark blue) gains in cases with (a) $\nu = 0$, (b) $\nu = 10^{-2}$, with maxima in both cases along $Re \cdot Er = k^2$ (white dashed line), where k increases in the direction of the arrow in (a). We fix $Re = 1$ and plot $|G|$ against Er along the black, dashed line in (a) for different viscosity ratios ν (colored) in (c), which shows four distinct peaks ①–④ at $Er = 0.14, 1.3, 4.27, 9.27$. Increasing viscosity decreases $|G|$ peaks, especially for ②, ③. Plotting the velocity profiles corresponding to ①–③ at $\nu = 0$ in (d–f) and $\nu = 10^{-2}$ in (g–i) reveals that they resemble harmonic standing waves within the solid. We confirm that these high gain results are indeed physical by plotting equivalent 2D DNS results as black scatter points in (d,g) where we notice agreement between the curves.

Lastly, 2D DNS simulations for $\nu = 0, 10^{-2}$ (Fig. 5d,f, black scatter points) validate our model predictions. Since it is numerically challenging to capture these high gain regimes, we propose $Re = 1$, $Er = 1.3$, $\nu = 0, 10^{-2}$ for benchmarking numerical simulations, in addition to the parameter sets presented in Section 4.4.

We have thus provided analytical solutions for the dynamics of a viscoelastic neo-Hookean solid immersed in an oscillatory Couette flow system. We have derived a general solution to account for arbitrary solid densities and viscosities in our setup, using two approaches—one in modal space generalizing the previous work of Sugiyama *et al.* (2011), and one in physical space. As a special limiting case, we recover the original solution of Sugiyama *et al.* (2011) for a density-matched solid with zero viscosity. Additionally, we recover analytical solutions

of single (Landau & Lifshitz 1987) and multi-fluid (Sim 2006; Leclaire *et al.* 2014) Stokes–Couette flows in the limit of zero solid elasticity. Further, our solutions compare well against DNS results (Fig. 3). They are found to exhibit a range of behaviors (Fig. 4), including high gains (Fig. 5), with potential applications in biophysics and engineering. Next, we discuss the case of a generalized Mooney–Rivlin solid, which presents higher order non-linear effects within the solid.

5. Generalization to Mooney–Rivlin solids

5.1. Modal semi-analytical solutions

In the case of a generalized Mooney–Rivlin solid, characterized by $c_3 \neq 0$, the hyperelastic stress is proportional to the cubic power of strain (Eq. 3.2) which signifies a higher order non-linear response to deformations. The resulting equations, whose non-linearity is overall captured via the parameter $c = c_3/c_1$, resist closed-form analytical solutions. Then, to investigate the system response in this setting, we derive a semi-analytical solution using the Fourier series machinery of Section 3.3.

The solution strategy here is to employ a Fourier pseudospectral collocation scheme (Sugiyama *et al.* 2011) for evaluating the nonlinear stress terms $\sigma_{\text{NL},k}$ in the governing Eq. 3.14, at a finite set of grid points $x_j = (j + \frac{1}{2})\Delta x$, with $\Delta x = L_s/K$. All other terms are treated as described in Section 3.3.

Armed with this spatial discretization, we employ a numerical time integration scheme to evolve the non-linear Eqs. (3.13) and (3.14). Here, we use a second order constant timestepper (of timestep Δt) comprised of mixed Crank–Nicolson (implicit, for stability in the viscous updates) and explicit Nyström (midpoint) rule for the second-order time derivatives (Hairer *et al.* 1991). If we denote the n^{th} time level $t = n\Delta t$ by a superscript n , then the prescribed wall velocity takes the analytical form

$$V_{\text{wall}}^{(n+1)} := V_{\text{wall}}((n+1)(\Delta t)) = \text{Im} \left[\hat{V}_{\text{wall}} \exp(i\omega ((n+1)\Delta t)) \right]. \quad (5.1)$$

For the interface displacement U_I and fluid velocity update in Eq. 3.13, we use the Crank–Nicolson scheme (Hairer *et al.* 1991)

$$U_I^{(n+1)} \approx U_I^{(n)} + \frac{\Delta t}{2} \left(V_I^{(n+1)} + V_I^{(n)} \right) + O(\Delta t^2) \quad (5.2)$$

and for updating the interface velocity V_I and solid displacements in Eq. 3.14, we utilize the explicit Nyström (midpoint) rule

$$\left(\frac{dV_I}{dt} \right)^{(n)} \approx \frac{V_I^{(n+1)} - V_I^{(n-1)}}{2\Delta t} + O(\Delta t^2).$$

Upon substituting these discretizations in the governing equations Eqs. (3.13) and (3.14), and by invoking the modal stress balance of Eq. 3.15 at every step, we obtain the solution, after standard (but tedious) algebraic manipulations. For brevity, we omit derivation details, which can be found in Supplementary Information ??.

5.2. Analysis of system behavior

We first validate our semi-analytical solutions against direct numerical simulations (Fig. 6) in the same setup of Fig. 3, but with $c = 4$ instead of zero. The choice of c is consistent with established biological tissue models (Raghavan & Vorp 2000). As can be seen in Fig. 6a, the solid velocity profiles exhibit characteristic high-curvature bends (marked), differently from the neo-Hookean case (Fig. 3) on account of the additional material non-linearity. Further,

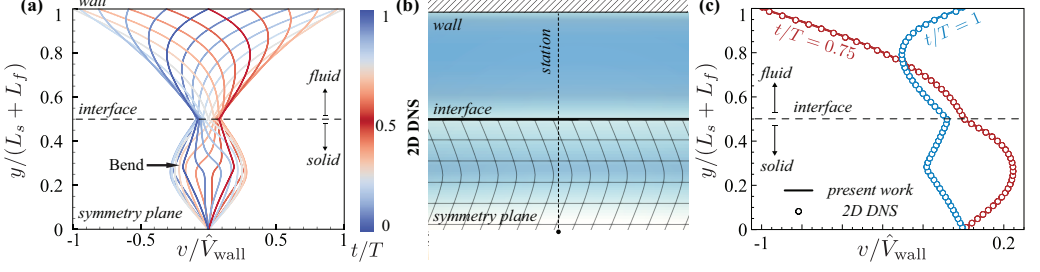


Figure 6: Comparison against simulations. (a) Non-dimensional semi-analytical velocity profiles in y , for a visco-elastic solid with a generalized Mooney–Rivlin model. The system response is shown only in the upper half plane. This system is characterized by $Re = 2$, $Er = 1$, $\nu = 0.1$, $c = c_3/c_1 = 4$, $\delta_f = 0.4$, $\delta_s = 0.126$, $\lambda = 0.225$. Additional details can be found in Supplementary Information ???. Colors indicate t/T . We also mark a high curvature bend in the profile with a black arrow. (b) We solve the above problem through 2D DNS (Bhosale *et al.* 2021) with corresponding simulation parameters reported in Supplementary Information ???. In this image, we mark the x -velocity field (orange/blue represent positive/negative velocity) and deformation contours within the solid, with the interface marked (black, thick solid) for visual clarity. Upon plotting the velocity profiles at the highlighted station (black, dashed) in the center of the domain, we see good agreement with our analytical results across all times as shown in (c). For the sake of clarity, we only show profiles at two different time instances. Here numerical results are plotted with scatter points whereas analytical results are plotted with a solid line.

as illustrated in Fig. 6c, our semi-analytical solutions are found to agree well with direct numerical simulations.

Next, in the spirit of Fig. 4, we highlight system responses upon varying both degree of solid non-linearity (c) and viscosity (Re). Throughout this exploration, we fix the elastic to viscous contributions by setting $Er = 1$ and $\nu = 0.1$. These values are informed by the rich dynamics of the central column of Fig. 4. We then span $c = [1, 5, 10] \times Re = [0.1, 0.5, 1, 2, 10]$ and report responses of the system in Fig. 7.

For solids with small c , we expect dynamics similar to the neo-Hookean counterpart, as the visco-elastic response is linear to a first order of approximation. This is confirmed from the solid zone profiles in the left column. Increasing the non-linearity coefficient stiffens the solid, constraining deformation velocities (narrower envelopes) as well as producing sharper bends (marked), as we move from left to right in Fig. 7.

Changing viscosity (Re) affects the response in a fashion similar to the neo-Hookean case (Fig. 4), where profile curvatures in both fluid and solid phases progressively get concentrated within sharper boundary layers, as we move from top to bottom in Fig. 7.

Finally, we investigate whether the high gain regimes seen in Section 4.5 exist for Mooney–Rivlin solids, and if so, under what conditions. Here, unlike Section 4.5, there is no mathematical guidance to identify high-gain parameters, thus we explore the phase space $Er - Re$ numerically for the representative cases $c = 1$ (Fig. 8a) and $c = 5$ (Fig. 8b). For $c = 1$, we see in Fig. 8a that high-gain peaks (bright yellow), although less pronounced, still occur in a regular structure that departs from the hyperbolae seen in the neo-Hookean case, and instead lie on the curve $Re \cdot Er^{0.5} = \text{constant}$. In Fig. 8c, we report the velocity profiles of a representative high gain case, and note that $|v/\hat{V}_{\text{wall}}|$ hardly exceeds 1, as opposed to the neo-Hookean cases of Fig. 5. As we increase c from 1 to 5, we observe that the peaks spread apart and gains further diminish (Fig. 8b). We conclude that the cubic non-linear term that characterize Mooney–Rivlin solids locally stiffens the material, reducing its propensity to deform and shear.

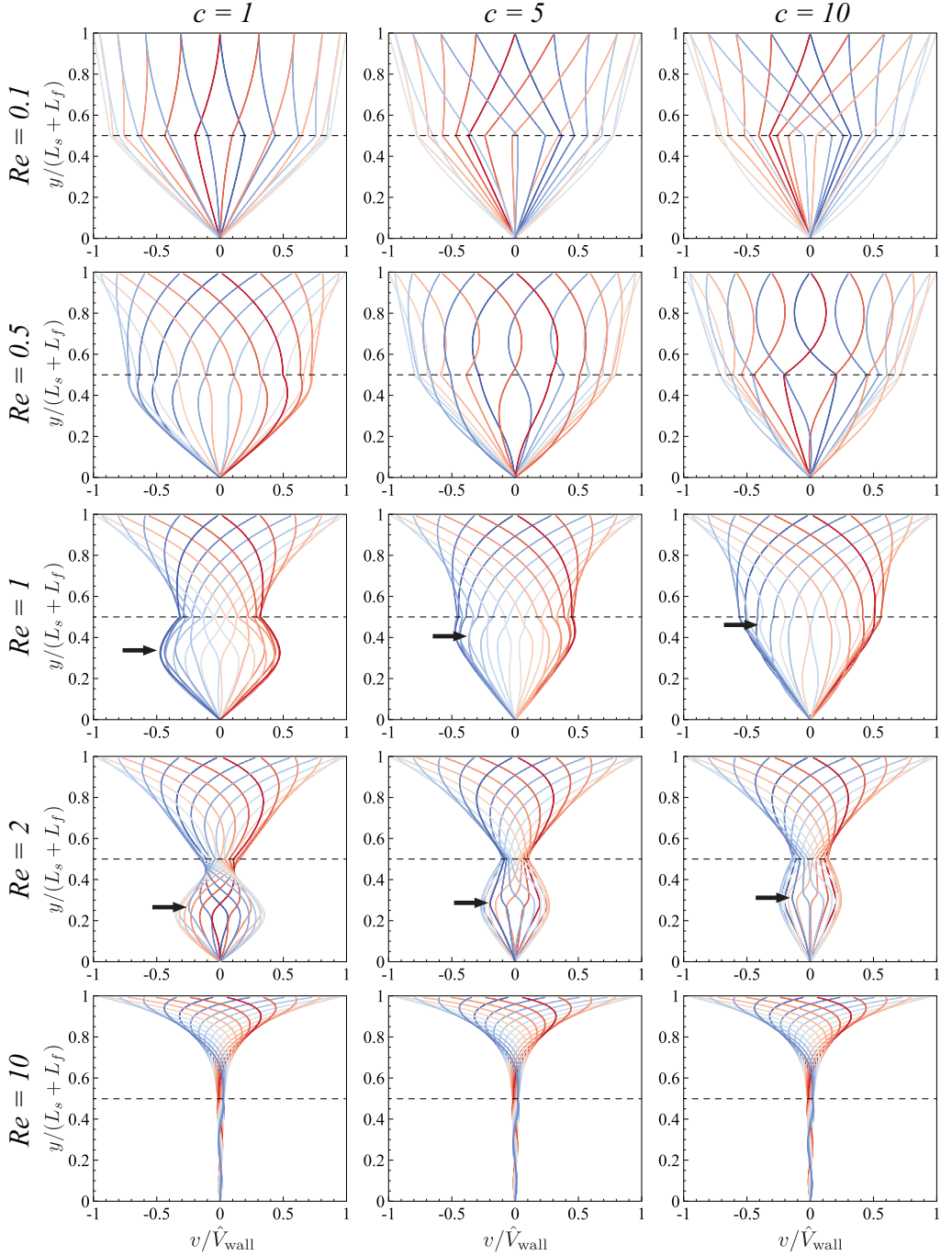


Figure 7: Dynamics with parametric variation. Non-dimensional velocity profile in y for parametric changes in $Re = [0.1, 0.5, 1, 2, 10] \times c = [1, 5, 10]$ with

$Er = 1, \nu = 0.1, \rho = 1$. The system response is shown only in the upper half plane. The black, dashed lines indicate the solid-fluid interface. Colors represent t/T , with the same colorbar as Fig. 2. We also mark the location of prominent high-curvature bends in the profiles with a black arrow.

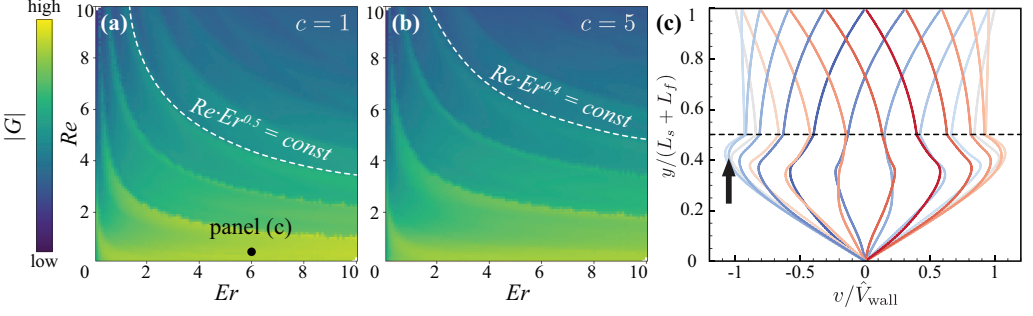


Figure 8: High amplitude gains for a Mooney–Rivlin solid. Phase map of numerically measured $|G|$ as a function of Re, Er for $\nu = 10^{-3}$ and (a) $c = 1$, (b) $c = 5$ shows regions of high (bright yellow) and low (dark blue) gains with maxima along $Re \cdot Er^{0.5} = \text{const}$ and $Re \cdot Er^{0.4} = \text{const}$ respectively, deviating from the hyperbolae seen in the neo-Hookean case. Velocity profiles of a representative case with $Re = 0.2, Er = 6, c = 1$ marked in (a) and plotted in (c) showcases high-gain bends (marked) characteristic of strong nonlinear effects in the solid.

6. Conclusion

We have presented solutions for an oscillatory Couette setup involving parallel viscoelastic solid–fluid layers sandwiched between two oscillating walls. We are motivated by the paucity of minimal yet representative (hyper-)elastohydrodynamic systems that can be analytically and rigorously analysed, given their relevance and ubiquity in biophysical and engineering settings. Here we consider visco-hyperelastic solids with arbitrary density and viscosity immersed in a Newtonian fluid. First, for a sandwiched viscous neo-Hookean solid, the governing equations simplify to an analytically tractable problem for which we derive two equivalent solutions. One is obtained by analytically solving the homogeneous Helmholtz equations derived from the governing PDEs. The other is based on partitioned Fourier-series expansions, providing a general machinery that can be applied to different material models. Obtained solutions, in the limit of zero elasticity, recover the classical Stokes–Couette solutions for single and multiple, immiscible fluids. Semi-analytic solutions for generalized Mooney–Rivlin materials are also derived, and numerically solved using a pseudospectral scheme, based on the partitioned Fourier-series expansions introduced in the neo-Hookean case. For both neo-Hookean and Mooney–Rivlin materials, we report quantitative agreement with direct numerical flow–structure interaction simulations, and further explore system behavior upon parametric changes in solid elasticity, fluid viscosity and higher order elastic nonlinearities. This analysis allows us to identify the spatio-temporal scales at play, assess the degree of flow–structure coupling, and highlight differences between neo-Hookean and Mooney–Rivlin models. We also highlight regimes of high solid phase displacements, which result from standing wave harmonics. The proposed hyperelastic oscillatory Couette system, and its analysis, can find application in a range of biophysical settings, from in-situ bio-film formation and synovial joint mechanics to solid-rheological characterization. Furthermore, the proposed setup may well serve as a benchmark to rigorously test numerical solvers for coupled fluid–elastic solid interactions. Finally, for building fundamental fluid mechanics intuition, we provide, as free software, an interactive, online sandbox demonstrating our results (Supplementary Information ??), together with our computational code.

7. Declaration of Interests

The authors report no conflict of interest.

REFERENCES

- ALBEN, SILAS, SHELLEY, MICHAEL & ZHANG, JUN 2002 Drag reduction through self-similar bending of a flexible body. *Nature* **420** (6915), 479–481.
- ALBEN, SILAS, SHELLEY, MICHAEL & ZHANG, JUN 2004 How flexibility induces streamlining in a two-dimensional flow. *Physics of Fluids* **16** (5), 1694–1713.
- ARGENTINA, MÉDÉRIC & MAHADEVAN, L 2005 Fluid-flow-induced flutter of a flag. *Proceedings of the National Academy of Sciences* **102** (6), 1829–1834.
- ARGENTINA, MEDERIC, SKOTHEIM, J & MAHADEVAN, L 2007 Settling and swimming of flexible fluid-lubricated foils. *Physical review letters* **99** (22), 224503.
- BAKKER, DEWI P, HUIJS, FRANK M, DE VRIES, JOOP, KLIJNSTRA, JOB W, BUSSCHER, HENK J & VAN DER MEI, HENNY C 2003 Bacterial deposition to fluoridated and non-fluoridated polyurethane coatings with different elastic modulus and surface tension in a parallel plate and a stagnation point flow chamber. *Colloids and Surfaces B: Biointerfaces* **32** (3), 179–190.
- BARTHES-BIESEL, DOMINIQUE 2016 Motion and deformation of elastic capsules and vesicles in flow. *Annual Review of fluid mechanics* **48**, 25–52.
- BHOSALE, YASHRAJ, ESMAILI, EHSAN, BHAR, KINJAL & JUNG, SUNGHWAN 2020 Bending, twisting and flapping leaf upon raindrop impact. *Bioinspiration & Biomimetics* **15** (3), 036007.
- BHOSALE, YASHRAJ, PARTHASARATHY, TEJASWIN & GAZZOLA, MATTIA 2021 A remeshed vortex method for mixed rigid/soft body fluid–structure interaction. *Journal of Computational Physics* p. 110577.
- BODNÁR, TOMÁŠ, GALDI, GIOVANNI P & NEČASOVÁ, ŠÁRKA 2014 *Fluid-structure interaction and biomedical applications*. Springer.
- BOWER, ALLAN F 2009 *Applied mechanics of solids*. CRC press.
- CARR, MARCUS E, SHEN, LINUS L & HERMANS, JAN 1976 A physical standard of fibrinogen: measurement of the elastic modulus of dilute fibrin gels with a new elastometer. *Analytical biochemistry* **72** (1-2), 202–211.
- CHRISTOV, IVAN C 2021 Soft hydraulics: from newtonian to complex fluid flows through compliant conduits. *arXiv preprint arXiv:2106.07164*.
- DI CARLO, DINO 2009 Inertial microfluidics. *Lab on a Chip* **9** (21), 3038–3046.
- DOWELL, EARL H & HALL, KENNETH C 2001 Modeling of fluid-structure interaction. *Annual review of fluid mechanics* **33** (1), 445–490.
- DOWSON, D & JIN, ZHONG-MIN 1986 Micro-elastohydrodynamic lubrication of synovial joints. *Engineering in medicine* **15** (2), 63–65.
- DUNCOMBE, TODD A, TENTORI, AUGUSTO M & HERR, AMY E 2015 Microfluidics: reframing biological enquiry. *Nature Reviews Molecular Cell Biology* **16** (9), 554–567.
- GAZZOLA, MATTIA, ARGENTINA, MÉDÉRIC & MAHADEVAN, LAKSHMINARAYANAN 2015 Gait and speed selection in slender inertial swimmers. *Proceedings of the National Academy of Sciences* **112** (13), 3874–3879.
- GROTBERG, JAMES B & JENSEN, OLIVER E 2004 Biofluid mechanics in flexible tubes. *Annu. Rev. Fluid Mech.* **36**, 121–147.
- GUIMARÃES, CARLOS F, GASPERINI, LUCA, MARQUES, ALEXANDRA P & REIS, RUI L 2020 The stiffness of living tissues and its implications for tissue engineering. *Nature Reviews Materials* **5** (5), 351–370.
- HAIRER, ERNST, NØRSETT, SYVERT P & WANNER, GERHARD 1991 *Solving ordinary differential equations I, Nonstiff problems*. Springer-Vlg.
- GAD-EL HAK, MOHAMED 2002 Compliant coatings for drag reduction. *Progress in Aerospace Sciences* **38** (1), 77–99.
- HEIL, MATTHIAS & HAZEL, ANDREW L 2011 Fluid-structure interaction in internal physiological flows. *Annual review of fluid mechanics* **43**, 141–162.
- HEIL, MATTHIAS, HAZEL, ANDREW L & SMITH, JACLYN A 2008 The mechanics of airway closure. *Respiratory physiology & neurobiology* **163** (1-3), 214–221.
- KOU, WENJUN, PANDOLFINO, JOHN E, KAHRILAS, PETER J & PATANKAR, NEELESH A 2017 Simulation studies of the role of esophageal mucosa in bolus transport. *Biomechanics and modeling in mechanobiology* **16** (3), 1001–1009.
- LANDAU, LD & LIFSHITZ, EM 1987 *Theoretical physics*, vol. 6, fluid mechanics.
- LECLAIRE, S, PELLERIN, N, REGGIO, M & TRÉPANIÉ, JY 2014 Unsteady immiscible multiphase flow validation of a multiple-relaxation-time lattice boltzmann method. *Journal of Physics A: Mathematical and Theoretical* **47** (10), 105501.

- LI, XUEJIN, VLAHOVSKA, PETIA M & KARNIADAKIS, GEORGE EM 2013 Continuum-and particle-based modeling of shapes and dynamics of red blood cells in health and disease. *Soft matter* **9** (1), 28–37.
- MIHAI, L ANGELA & GORIELY, ALAIN 2017 How to characterize a nonlinear elastic material? a review on nonlinear constitutive parameters in isotropic finite elasticity. *Proceedings of the Royal Society A: Mathematical, Physical and Engineering Sciences* **473** (2207), 20170607.
- NALIM, RAZI, PEKKAN, KEREM, SUN, HUI BIN & YOKOTA, HIROKI 2004 Oscillating couette flow for in vitro cell loading. *Journal of biomechanics* **37** (6), 939–942.
- POZRIKIDIS, CONSTANTINE 2003 *Modeling and simulation of capsules and biological cells*. CRC Press.
- RAGHAVAN, ML & VORP, DAVID A 2000 Toward a biomechanical tool to evaluate rupture potential of abdominal aortic aneurysm: identification of a finite strain constitutive model and evaluation of its applicability. *Journal of biomechanics* **33** (4), 475–482.
- SIM, WOO-GUN 2006 Stratified steady and unsteady two-phase flows between two parallel plates. *Journal of mechanical science and technology* **20** (1), 125.
- SONG, FANGCHAO, KOO, HYUN & REN, DACHENG 2015 Effects of material properties on bacterial adhesion and biofilm formation. *Journal of dental research* **94** (8), 1027–1034.
- SUGIYAMA, KAZUYASU, II, SATOSHI, TAKEUCHI, SHINTARO, TAKAGI, SHU & MATSUMOTO, YOICHIRO 2010 Full eulerian simulations of biconcave neo-hookean particles in a poiseuille flow. *Computational Mechanics* **46** (1), 147–157.
- SUGIYAMA, KAZUYASU, II, SATOSHI, TAKEUCHI, SHINTARO, TAKAGI, SHU & MATSUMOTO, YOICHIRO 2011 A full eulerian finite difference approach for solving fluid–structure coupling problems. *Journal of Computational Physics* **230** (3), 596–627.
- SUN, HUI B 2010 Mechanical loading, cartilage degradation, and arthritis. *Annals of the New York Academy of Sciences* **1211** (1), 37–50.
- SUN, HUI BIN, NALIM, RAZI & YOKOTA, HIROKI 2003 Expression and activities of matrix metalloproteinases under oscillatory shear in il-1-stimulated synovial cells. *Connective tissue research* **44** (1), 42–49.
- TYTELL, ERIC D, LEFTWICH, MEGAN C, HSU, CHIA-YU, GRIFFITH, BOYCE E, COHEN, AVIS H, SMITS, ALEXANDER J, HAMLET, CHRISTINA & FAUCI, LISA J 2016 Role of body stiffness in undulatory swimming: insights from robotic and computational models. *Physical Review Fluids* **1** (7), 073202.
- VELVE-CASQUILLAS, GUILHEM, LE BERRE, MAËL, PIEL, MATTHIEU & TRAN, PHONG T 2010 Microfluidic tools for cell biological research. *Nano today* **5** (1), 28–47.
- VLAHOVSKA, PETIA M & GRACIA, RUBEN SERRAL 2007 Dynamics of a viscous vesicle in linear flows. *Physical Review E* **75** (1), 016313.
- WANG, XIAOJIA & CHRISTOV, IVAN C 2019 Theory of the flow-induced deformation of shallow compliant microchannels with thick walls. *Proceedings of the Royal Society A* **475** (2231), 20190513.
- WU, PEI-HSUN, AROUSH, DIKLA RAZ-BEN, ASNACIOS, ATEF, CHEN, WEI-CHIANG, DOKUKIN, MAXIM E, DOSS, BRYANT L, DURAND-SMET, PAULINE, EKPENYONG, ANDREW, GUCK, JOCHEN, GUZ, NATALIA V & OTHERS 2018 A comparison of methods to assess cell mechanical properties. *Nature methods* **15**, 491–498.
- ZHU, DONG & JANE WANG, Q. 2011 Elastohydrodynamic lubrication: A gateway to interfacial mechanics—review and prospect. *Journal of Tribology* **133** (4).